




# Numerical study of the Richtmyer–Meshkov instability of a three-dimensional minimum-surface featured $\text{SF}_6$ /air interface

Cite as: Phys. Fluids **32**, 024108 (2020); <https://doi.org/10.1063/1.5141783>

Submitted: 08 December 2019 • Accepted: 31 January 2020 • Published Online: 18 February 2020

 Ben Guan (关奔),  Dayi Wang (王大一),  Ge Wang (王革), et al.



View Online



Export Citation



CrossMark

## ARTICLES YOU MAY BE INTERESTED IN

[Microscopic Richtmyer–Meshkov instability under strong shock](#)

Physics of Fluids **32**, 024109 (2020); <https://doi.org/10.1063/1.5143327>

[Numerical study on shock-accelerated gas rings](#)

Physics of Fluids **32**, 026102 (2020); <https://doi.org/10.1063/1.5135762>

[Turbulent transport and mixing in the multimode narrowband Richtmyer–Meshkov instability](#)

Physics of Fluids **31**, 096105 (2019); <https://doi.org/10.1063/1.5111681>

APL Machine Learning

Open, quality research for the networking communities

MEET OUR NEW EDITOR-IN-CHIEF

LEARN MORE



# Numerical study of the Richtmyer–Meshkov instability of a three-dimensional minimum-surface featured SF<sub>6</sub>/air interface

Cite as: Phys. Fluids 32, 024108 (2020); doi: 10.1063/1.5141783

Submitted: 8 December 2019 • Accepted: 31 January 2020 •

Published Online: 18 February 2020



Ben Guan (关奔),<sup>1</sup> Dayi Wang (王大一),<sup>1</sup> Ge Wang (王革),<sup>1,a)</sup> E. Fan (范镔),<sup>2</sup>   
and Chih-Yung Wen (温志湧)<sup>2</sup>

## AFFILIATIONS

<sup>1</sup>College of Aerospace and Civil Engineering, Harbin Engineering University, Harbin 150001, China

<sup>2</sup>Department of Mechanical Engineering and Interdisciplinary Division of Aeronautical and Aviation Engineering, The Hong Kong Polytechnic University, Kowloon 999077, Hong Kong, China

<sup>a)</sup>Author to whom correspondence should be addressed: wangge@hrbeu.edu.cn

## ABSTRACT

The Richtmyer–Meshkov instability of a three-dimensional (3D) minimum-surface featured SF<sub>6</sub>/air interface subjected to a planar weak incident shock is numerically studied. The focus is placed on presenting more intuitive details of the complex shock-interface interactions. In the present work, 3D Euler equations are solved. The fifth-order weighted essentially non-oscillatory scheme and the level-set method combined with the real ghost fluid method are adopted. The gas interface morphologies are precisely reproduced according to the previous experimental images, the wave systems in 3D space are illustrated, and the velocity distribution in a characteristic plane is depicted. Based on which, the unknown lagging structure in the previous experiment can be reasonably explained. It is actually the soap fog driven by the flow field. The baroclinic vorticity generation and the perturbation amplitude growth histories are measured. The present numerical study well confirms the 3D curvature effect and supports the extended 3D theoretical model for the heavy/light interface scenario.

Published under license by AIP Publishing. <https://doi.org/10.1063/1.5141783>

## I. INTRODUCTION

When an interface between two different fluids is impulsively accelerated, the perturbation of the interface will grow with time, the interface loses its stability and evolves into a final turbulent flow. This kind of interface instability is called Richtmyer–Meshkov instability (RMI), which was first introduced theoretically by Richtmyer<sup>1</sup> and experimentally confirmed by Meshkov.<sup>2</sup> The RMI, as a fundamental physical mechanism, occurs widely in both artificial and natural phenomena, such as supersonic combustion of scramjets,<sup>3</sup> supernova explosion,<sup>4</sup> and applications of inertial confined fusion.<sup>5</sup> Besides, many research studies targeting on the RMI has promoted the understanding of vortex dynamics, shock wave interactions, and turbulent mixing, improved the experimental techniques, and so on. As a result of all these backgrounds, the RMI has been extensively studied in recent years using a variety of experimental, numerical, and theoretical methods. Several comprehensive reviews on

RMI have been presented by Zabusky,<sup>6</sup> Brouillette,<sup>7</sup> and Ranjan *et al.*<sup>8</sup>

Most of the early RMI studies concentrate on two-dimensional (2D) configurations due to their easy implementation in experimental operations and simple mathematical expressions. Typical 2D configurations cover the 2D single-mode interface<sup>9–13</sup> and gas cylinders<sup>14–18</sup> although in different scales. By applying the soap film techniques, researchers performed many shock tube experiments on the RMI of different types of polygonal gas cylinders,<sup>18–21</sup> V-shaped interfaces,<sup>22,24</sup> single-mode,<sup>25</sup> and saw-tooth interfaces.<sup>26</sup> Comparing to the 2D configurations, the amount of three-dimensional (3D) cases are apparently limited because the 3D interfaces are more difficult to be well controlled and visualized in experiments and because they consume huge memory resources in computations. The most easily produced and well-controlled 3D interface is soap bubbles,<sup>14,27,28</sup> their interface morphologies were found to be an extended analog to the 2D cylinders. 3D single-mode RMI, as a

basic configuration, has been given in-depth investigation through the years.<sup>29–31</sup> On a macroscopic level, quasi-randomly perturbed multi-mode interfaces<sup>32–35</sup> are used to take the turbulent element into account. The 3D effect of a vertical gas jet<sup>36</sup> and gas cylinder<sup>37</sup> in experiments were discussed in detail using numerical simulations.

Inspired by Krechetnikov<sup>38</sup> who emphasized the importance of the interface curvature effect on RMI, Luo *et al.*<sup>39,40</sup> recently conducted a series of shock tube experiments concentrating on the curvature effects of a 3D single-mode gas interfaces (GI). By applying their advanced soap film techniques, they produced a well-defined 3D single-mode soap film to initially separate different gases. Due to the natural minimum-surface property of the soap film, this single-mode soap film suffers from great 3D effect caused by the two principal curvatures on every position of the film, which have the same magnitude but opposite signs. When this minimum-surface featured interface was used in RMI experiments, it was found that the opposite curvature significantly mitigates the single-mode amplitude growth rate comparing to the 2D impulsive model. An extended 3D linear theoretical model was also proposed to well estimate the interface amplitude growth in experiments. Based on these early experimental works, Luo *et al.*<sup>41,42</sup> also conducted numerical studies to reveal more details in the complex shock-interface interactions of this light/heavy scenarios. Their numerical studies further proved the curvature effect on the RMI and presented the thought of using curvature arrangement as a way to manipulate the instability evolution.

Interestingly, in the experimental images of the SF<sub>6</sub>/air scenario, there exists an abnormal structure lagging behind the gas interface (labeled as S1 in Ref. 40). This S1 was described as a region of density variation. However, a final conclusion on its formation could not be given at that time and it was waiting for a numerical interpretation. As a result of this, the purpose of the present work is to provide the numerical results according to the previous SF<sub>6</sub>/air experiment, to demonstrate more hidden details in the complex 3D shock-interface interactions. A comprehensive and intuitive landscape is to be completed by supplementing the present work to the whole study series on the minimum-surface RMI of both the light/heavy and heavy/light scenarios. Moreover, the interpretation of the S1 formation could fill the gap between the experimental and numerical results so that other researchers could have more confidence in using our experimental results for their future studies.

## II. NUMERICAL METHODS

As the present study focuses on the interaction between a weak shock wave and a gas interface at its early stage, the viscosity plays a minor role so that the viscous effect, the boundary layer effect, and the turbulent mixing can all be reasonably neglected. We use exactly the same numerical methods as those of Ref. 41 in which 3D Euler equations were solved to reproduce the air/SF<sub>6</sub> interface evolution after it was impacted by a shock wave. The ideal gas law as the equation of state is employed to complete the mathematical description. Again, in a Cartesian coordinate system, the level set method<sup>43</sup> and the real ghost fluid method<sup>44</sup> are used to represent the interface, which separates the different gases. This treatment produces a sharp interface in the computation so that diffusion between the gases is totally neglected. Both the governing equations and the

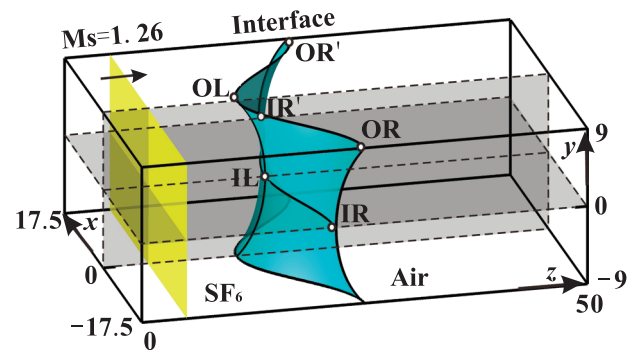


**FIG. 1.** Initial settings of the shock-accelerated minimum-surface featured SF<sub>6</sub>/air single-mode interface. IR', IL, IR and OR', OL, OR (I, inner; O, outer; L, left; R, right) denote the characteristic positions of the troughs and crests of the initially perturbed interface at  $y = 0$  mm and 9 mm, respectively.

level set function are solved by fifth-order weighted essentially non-oscillatory scheme<sup>45</sup> in uniform cubic cells and advanced in time by the third-order Runge–Kutta method.

To be consistent with our previous experimental settings and be comparable with our early simulations on air/SF<sub>6</sub> cases, the present numerical settings and nomenclatures of SF<sub>6</sub>/air simulation are held identical as those in Ref. 41 (with a single wave length shown in Fig. 1). The simulated initial gas interface (cyan colored) has an initial amplitude of  $a_o^0 = 5$  mm at the top and bottom boundaries (i.e.,  $y = \pm 9$  mm, line OR'-OL-OR) and has an initial amplitude of  $a_i^0 = 1.79$  mm at the symmetry plane ( $y = 0$  mm, line IR'-IL-IR). The horizontal wavelength is  $\lambda = 35$  mm and wave number  $k = 2\pi/\lambda$ . This interface configuration is defined by the minimum-surface property.<sup>46</sup> In each  $xz$  plane, the initial interface can be characterized by

$$z = f(y) \cos(kx), y \in [-9, 9]$$

and

$$y = \pm \int_{a_i}^{f(y)} \frac{dx}{\sqrt{e^{k^2(x^2 - a_i^2)} - 1}},$$

where the plus (minus) sign stands for  $y > 0$  ( $y < 0$ ).

The computation domain is confined in the upper left quarter with a cuboid shape of 17.5 mm  $\times$  9 mm  $\times$  100 mm due to the symmetric property of the physical space under consideration. In order to make sure the present study well reproduces the experimental observations, three initial setting parameters, i.e., the incident shock Mach number and SF<sub>6</sub> volume fractions on both sides of the initial gas interface, are finely tuned within their respective error ranges. The finally determined incident shock strength is  $Ms = 1.26$ , and there is 88% of the SF<sub>6</sub> volume fraction on the upstream (left) side of the initial interface, while 16% of SF<sub>6</sub> on the downstream (right) side of the initial gas interface. It indicates that there were leakage or residual SF<sub>6</sub> gas in the downstream part of the test section in the experimental implementation. The pre-shock flow field is set to be stationary and the post-shock flow variables are computed by the Rankine–Hugoniot relations. The boundary conditions on the six surfaces of the computation cuboid include four symmetric boundaries ( $x = 17.5$  mm,  $y = 9$  mm,  $x = 0$  mm, and  $y = 0$  mm) and two

outflow boundaries ( $z = 0$  mm and  $z = 100$  mm). The outflow conditions are enforced by applying zeroth-order extrapolation to the boundaries. The effects of the mesh size on the numerical accuracy are evaluated in advance and the number of grid cells is finally considered to be  $175 \times 90 \times 1000$ , which corresponds to a uniform grid size of  $\Delta x = \Delta y = \Delta z = 0.1$  mm. Further validations of the present numerical methods can be found in Refs. 41 and 42.

### III. RESULTS AND DISCUSSION

#### A. Comparison with experiment

Figure 2 shows the comparison of the present numerical results with our previous experimental images at different instants. The numerical density values at each instant are integrated along the  $y$ -direction and the first-order derivative of the integrated density is calculated to resemble the knife-edge setup in the experimental schlieren system. The characteristic positions of the gas interface in Fig. 1 can be found here in the inset of time  $0 \mu\text{s}$ . When part of the incident shock goes through the gas interface (at  $50 \mu\text{s}$ ), a fast moving and divergent transmitted shock (TS) to the downstream side as well as a reflected rarefaction (RR) to the upstream side are clearly seen. The 3D feature of the initial gas interface leads to distinct 3D TS

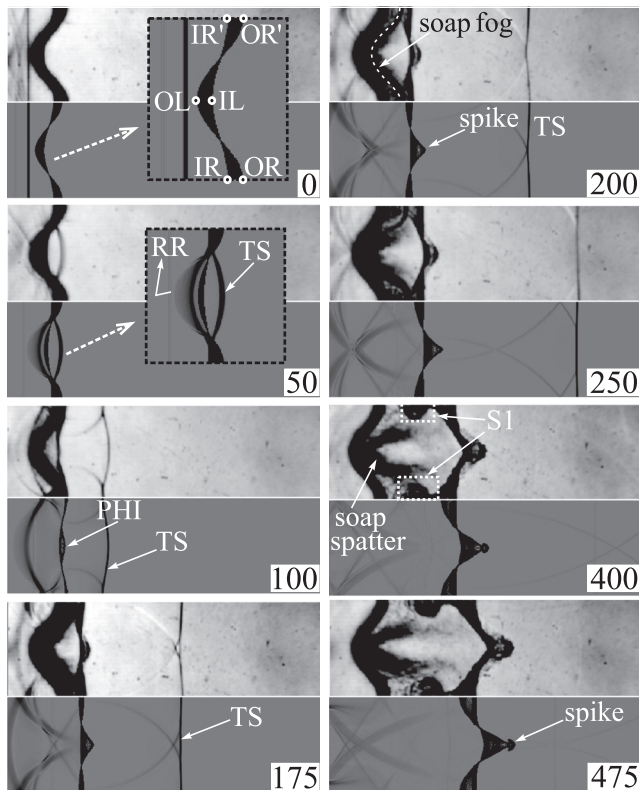


**FIG. 2.** The comparison between experimental and numerical schlieren images during the evolution of a shock-accelerated minimum-surface featured  $\text{SF}_6$ /air interface. The top halves are experimental schlierens and the bottom halves are numerical results. TS: transmitted shock, RR: reflected rarefaction, and PHI: phase inversion.

and RR fronts. In the schlieren images, this 3D feature of the waves appears as the thickened shock front and widened rarefaction wave. At  $100 \mu\text{s}$ , both the TS and RR are leaving the interface. The gas interface, at this moment, is clearly seen to be contracted. Its unevenness can only be detected from the phase inversion (PHI) part in the middle area. The TS gradually recovers its original planeness as it further propagates downstream and the interface amplitude is growing ( $175 \mu\text{s}$ ).

From  $200 \mu\text{s}$  to  $250 \mu\text{s}$ , except the growing of the interface amplitude, a salient feature of the experimental images is the detachment of the gas interface and the soap film. As has been proved in a series of previous studies,<sup>23,47,48</sup> the soap film, once impacted by a shock wave, ruptures and atomizes immediately. It exerts very limited influence on the later flow field. To be accurate, the liquid soap at this moment appears as atomized soap fog (as depicted by the white dashed curve). This kind of detachment can be observed frequently in heavy/light gas interface scenarios.<sup>18,23</sup>

Interestingly, seen at  $400 \mu\text{s}$ , distinct lagging structures (S1, as highlighted by white dashed squares) are formed. In our previous study,<sup>36</sup> we believed that S1 was caused by gas interface deformations, the present numerical results deny our previous judgment. There is no density structures lagging behind the gas interface in the numerical image. The present numerical results agree with our common sense toward a heavy/light gas interface scenario. The behavior of the soap fog is apparently subjected to the 3D effect making it move vertically (in  $y$ -direction). From the experimental images at  $400 \mu\text{s}$  and  $475 \mu\text{s}$ , it can be reasonably speculated that the middle part of the soap fog is spattered onto the visualizing window, while the other parts are entrained by the gas flow and deform into the S1 structure. More details are discussed in Secs. III B–III F.

#### B. Three-dimensional interface morphology

Focusing on the interface morphology, 3D views of the interface evolution at  $0 \mu\text{s}$ ,  $100 \mu\text{s}$ , and  $475 \mu\text{s}$  are depicted in Fig. 3. After the gas interface is shocked (see  $100 \mu\text{s}$ ), the interface amplitude experiences obvious contraction. Judging from the upper boundary (plane  $y = 9$  mm) and the lateral boundary (plane  $x = -17.5$  mm), the interface is also undergoing phase inversion. In the following stage, the amplitude of the inversed interface grows as time elapses. The original left-most point OL becomes the right-most protrusion (at  $100 \mu\text{s}$ ) and then further develops into a downstream spike (at  $475 \mu\text{s}$ ). In the meanwhile, the original right-most four corners become the left-most bubbles. In a whole, the interface finally turns into an inversed typical “bubble-spike” instability geometry.

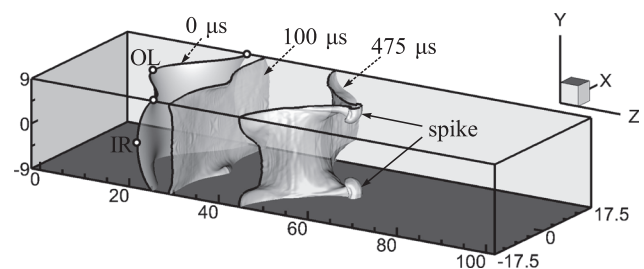


**FIG. 3.** Numerical results of the 3D gas interface at different moments.



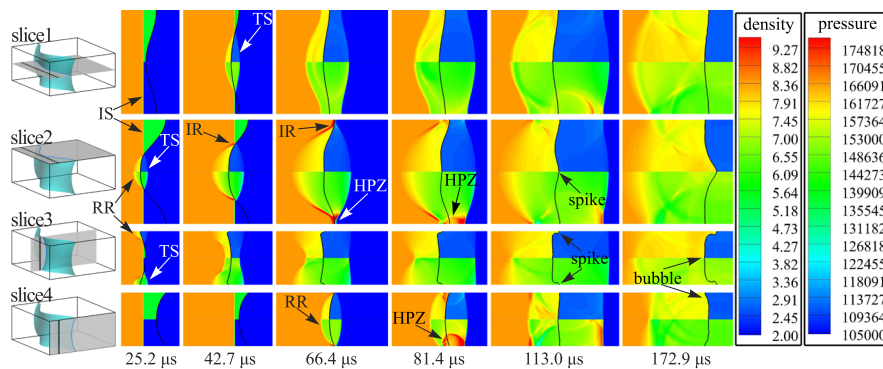


**FIG. 4.** Wave patterns in characteristic slices. Positions of the characteristic slices are shown in the first column as slice1 ~ slice4. Wave pattern sequences of each slice are listed in corresponding rows with time labeled at bottom. In each inset, the upper half depicts the density contour, while the lower half depicts the pressure contour. IS: incident shock, TS: transmitted shock, RR: reflected rarefaction, IR: irregular rarefaction, and HPZ: high-pressure zone.

### C. Wave systems

Wave systems on four characteristic planes (slice1 ~ slice4) are depicted in order to uncover the detailed shock-interface interactions, as shown in Fig. 4. Here, slice1 is the plane  $y = 0$  mm, slice2 is  $y = 9$  mm, slice3 is  $x = 0$  mm, and slice4 is  $x = -17.5$  mm (first column in Fig. 4). It is seen that the incident shock (IS) touches but not completely over-sweeps the whole gas interface at  $25.2 \mu\text{s}$ ; only the upper and lower boundary parts are shocked at this moment (see slice2 and slice3). 3D divergent TS and RR are observed. At  $42.7 \mu\text{s}$ , the amplitude of the interface are experiencing strong compression except slice4, which has not touched by the IS yet. Interestingly, from slice2, irregular reflection (IR) is formed as the IS incident angle increases. Other than a centered rarefaction wave, the reflected waves are composed of a thin high-pressure layer followed by a low-pressure rarefaction zone. At  $66.4 \mu\text{s}$ , the IS processes the whole gas interface (GI). The high-pressure layer formed by the IR is focusing toward the computation domain corner (slice2) causing a high-pressure zone (HPZ). This HPZ expands at  $81.4 \mu\text{s}$  and all the waves leave the GI at the following moments ( $113.0 \mu\text{s}$  and  $172.9 \mu\text{s}$ ). The most pronounced phase inversion is demonstrated in slice2 where the largest initial amplitude exists. The original upstream-most characteristic point OL becomes the downstream spike tips.

To give an intuitive demonstration of the 3D wave structures, especially the development of the high-pressure layers and zones caused by the IR, the positions of key wave structures and the GI (colored in cyan) are demonstrated in Fig. 5. The wave structures are represented by pressure isosurfaces. Bright colors (e.g., yellow and red) are assigned to the pressure isosurfaces so as to make them distinguishable. As seen, the high-pressure layers appear as curved bands connecting the GI and the upstream RR ( $42.7 \mu\text{s}$ ). With the TS and the RR leaving the GI, the two high-pressure layers get closer (see  $66.4 \mu\text{s}$ ). At this moment, the high-pressure layers focus at the computation domain corners forming the HPZs. The 3D features can also be detected from the expansion of HPZs ( $81.4 \mu\text{s}$ ) when the expanding shock fronts move both vertically and horizontally. At  $113.0 \mu\text{s}$ , the main waves are far from the GI and the HPZs do not exert direct influence on the GI any more.

### D. Interpretation of structure S1

The wave structure development apparently affects the velocity field in the 3D space. The movement of the high-pressure layers and zones of  $\text{SF}_6$  induced by IR induce the vertical and lateral flow velocities on the upstream side of the GI (see Fig. 5). Consequently, the soap fog that trails behind the GI can be severely influenced. Figure 6

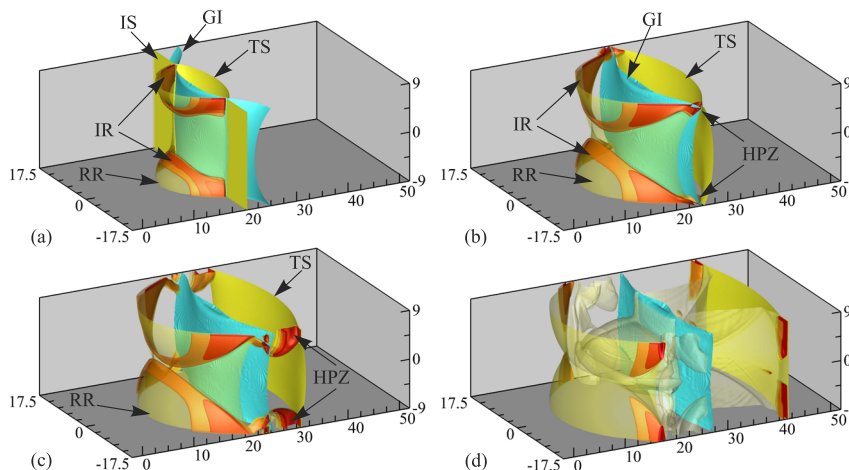


**FIG. 5.** 3D wave structures at (a)  $42.7 \mu\text{s}$ , (b)  $66.4 \mu\text{s}$ , (c)  $81.4 \mu\text{s}$ , and, (d)  $113.0 \mu\text{s}$ . IS: incident shock, GI: gas interface, TS: transmitted shock, IR: irregular reflection, RR: reflected rarefaction, and HPZ: high-pressure zone.

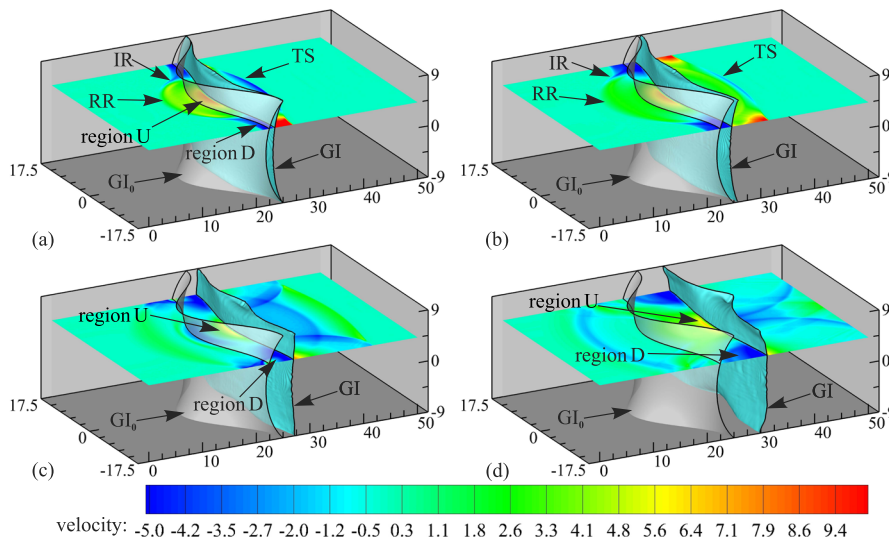


**FIG. 6.** Vertical velocity distribution of plane  $y = 4.5$  mm at (a)  $66.4 \mu\text{s}$ , (b)  $81.4 \mu\text{s}$ , (c)  $113.0 \mu\text{s}$  and, (d)  $172.9 \mu\text{s}$ . Region U stands for the region with positive velocity in  $y$ -direction, while region D stands for the region with negative velocity in  $y$ -direction. TS: transmitted shock, RR: reflected rarefaction, IR: irregular reflection, GI: gas interface,  $GI_0$ : initial gas interface.

extracts the vertical velocity ( $v$ ) distribution in  $y = 4.5$  mm plane at four moments. Together with the velocity distribution slice, the instant interface position (GI) and the initial intact interface position ( $GI_0$ ) are also depicted in order for the reader to anchor the detached soap fog between them.

Clearly, seen at  $66.4 \mu\text{s}$ , there are various flow directions for  $\text{SF}_6$  at the upstream side of the GI. The middle part (labeled as region U) moves upward following the left-going RR, while the two lateral parts (region D) move downward following the IR induced high-pressure layers and zones. Going through the four moments, the GI leaves its original position  $GI_0$ , the downstream wave TS and upstream RR separate further apart, and the high-pressure zones eventually disappear (see  $172.9 \mu\text{s}$ ), while the velocity pattern upstream of the GI does not change.

Combining this velocity distributions and the above wave pattern demonstrations, it is quite clear that during this early stage, the  $\text{SF}_6$  gas in the middle region U is driven upwards, while the lateral region D is driven downwards to the lateral middle part

( $x = \pm 17.5$  mm,  $y = 0$  mm). Consequently, the middle part of the soap fog (in region U) is driven to the upper boundary and the lateral parts of the soap fog (in region D) are driven to the lateral middle region. This explains the motion of the soap fog in the experimental images in Fig. 2; in other words, the middle part of the soap fog was spattered onto the visualizing window (soap spatter), while the lateral two parts were evolved into the image structures in the S1 regions.

### E. Vorticity distribution

The distributions of the normal component of the vorticity in four characteristic planes at time  $66.4 \mu\text{s}$  and  $113.0 \mu\text{s}$  are shown in Fig. 7. At  $66.4 \mu\text{s}$ , the TS just over-sweeps the whole GI and the vorticity is deposited initially. On the two horizontal slices (slice1 and slice2), the vorticity promotes the interface phase inversion. Apparently in slice2, the large amplitude of the interface deposits large vorticity. However, the vorticity deposition in the two vertical slices

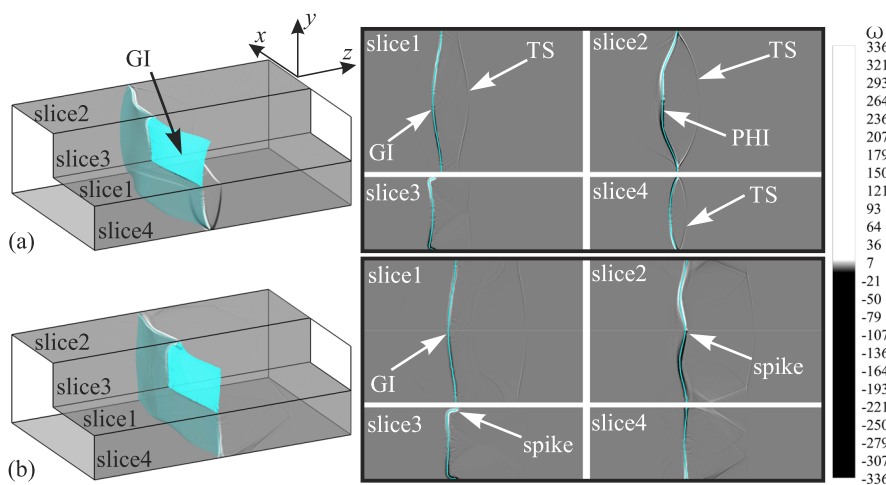


**FIG. 7.** Vorticity distributions on four characteristic slices at (a)  $66.4 \mu\text{s}$  and (b)  $113.0 \mu\text{s}$ . GI: gas interface, TS: transmitted shock, PHI: phase inversion.

play opposite roles in affecting the interface phase inversion of slice1. In other words, slice3 depresses and slice4 promotes the interface phase inversion. Due to this complex vorticity influence, the interface amplitude in slice1 has a very slow changing rate. At  $113.0 \mu\text{s}$ , the phase inversion in slice1 has not completed yet. On the contrary, the formation of spikes in slice2 and slice3 are nearly done. Worth noting is that, in the following stage, the vorticity holds this distribution pattern. On the interface amplitude growth of slice1, the vorticity in slice1 and slice3 always play opposite roles; one promotes and the other depresses. Eventually, the non-consistent vorticity effect will express itself in the amplitude histories.

## F. Amplitude growth

To quantitatively reveal the 3D curvature effect and to numerically testify the reliability of the extended 3D theoretical model for the heavy/light scenario proposed by Luo *et al.*,<sup>39</sup> three typical interface geometries are examined. The three interface geometries are the 3D single-mode interface (3D+), 2D single-mode interface (2D), and the present minimum-surface featured single-mode interface (3D− for short), as shown in Fig. 8. The 3D+ have two identical principal curvatures, the 2D have one zero-valued principal curvature, and the 3D− have two opposite signed principal curvatures. All of these three geometries have identical initial amplitude  $a_i^0 = 1.79 \text{ mm}$  and wave number  $k$  in their horizontal middle plane (the red lines), while in the vertical middle plane, the different principal curvature comes into play (the blue lines). Mathematically, the 3D+ and 2D interfaces can also be described by  $z = f(y)\cos(kx)$ . The only difference is that the initial amplitude function is  $f(y) = a_i^0 \cos(ky)$  for the 3D+ case and  $f(y) = a_i^0$  for the 2D scenario.

In Fig. 9, the amplitude growth histories of the middle horizontal plane in all geometries (red lines in Fig. 8) are extracted to make a comparison. The quantities are normalized as  $\bar{a} = ka_i^t$  and  $\tau = kv_i(t - t_0)$ , where the  $a_i^t$  is the evolving interface amplitude at time  $t$ ,  $t_0$  is the time when the amplitude reaches the minimum value, and  $v_i$  represents the initial perturbation growth rate in the linear phase for the present 3D− interface. According to the analysis of Meyer and Blewett<sup>9</sup> for a heavy/light interface, the extended 3D linear growth rate  $v_i$  can be formulated as  $v_i = \frac{1}{2}(2 - \sqrt{2})(1 + Z_c)ka_i A^+ \Delta v$ , in which  $Z_c = 1 - \Delta v/W_s$  is the compression factor,  $\Delta v$  is the interface velocity jump after shock,  $W_s$  is the incident shock velocity, and  $A^+$  is the post-shock Atwood number. Deriving from the above treatment, the growth rate is  $\frac{\sqrt{2}}{2-\sqrt{2}}v_i$  for the 3D+ and  $\frac{1}{2-\sqrt{2}}v_i$  for the 2D

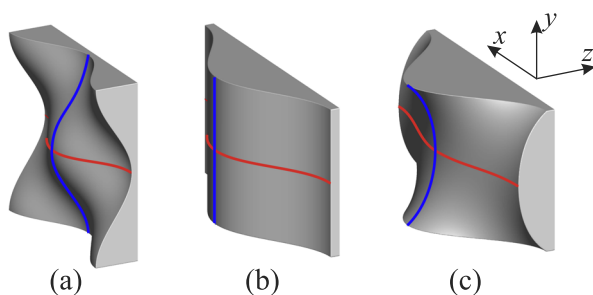


FIG. 8. Initial interface geometries of (a) 3D+, (b) 2D, and, (c) 3D−.

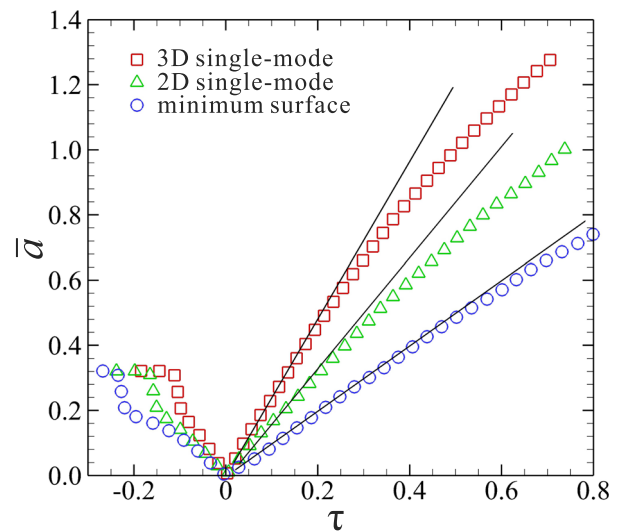


FIG. 9. Amplitude growth histories of 3D single-mode interface (3D+, squares), 2D single-mode interface (2D, triangles) and, the present minimum surface (3D−, circles). The black solid lines denote the theoretical impulsive growth predictions of the three cases.

interface. Figure 9 apparently shows that, the amplitude of the 3D+ interface grows the fastest among the three, the 2D one is in the second place, and the present 3D− interface grows the slowest. The theoretical impulsive growth predictions (shown as the three solid black lines) reliably agree with the present numerical results in the early linear range. The opposite curvatures not only lower down growth rate but also extend the linear stage of the 3D− interface evolution. In this case, the valid prediction time of the theoretical impulsive model is seen much longer for the 3D− case than the other two.

## IV. CONCLUSION

The RMI of a shock-accelerated 3D minimum-surface featured single-mode interface (3D−) is numerically studied in the present work. The precise adjustment of the initial parameter settings ensures the excellent agreement between the present numerical results and the previous experimental images. Based on this, the complex shock-interface interaction is demonstrated in-depth. Not only the density and pressure distributions in the characteristic slices but also the wave structures in 3D views are illustrated. It is found that the irregular reflection of the incident shock plays a key role in affecting the interface morphology as well as the detached soap fog trailing behind the real gas interface. The induced velocity field by the shock reflection on the upstream side of the gas interface spatters part of the soap fog onto the visualizing window, while it drives the rest of the atomized soap mists into the middle area of the 3D space causing the soap fog to flow with the  $\text{SF}_6$  gas for a long distance. It reasonably explains the formation of the unknown structure S1 appeared in the previous experiments, so that the gap between the experimental images and the numerical results is filled. The vorticity is mainly deposited on the gas interface and dominates the following morphology after the shock leaves the interface. The amplitude growth histories of three typical interfaces in their characteristic

planes, namely, the 3D+, 2D, and the present 3D–interfaces, are extracted and compared. The growth histories numerically prove the curvature effect. That is, same-signed principal curvatures promote the interface amplitude growth, while opposite-signed principal curvatures depress it. The amplitude growth histories also numerically support the reliability of the extended 3D theoretical model for the heavy/light scenarios. This research clearly elucidates that the 3D effect of the interface, and the role of the induced soap fog movement played in the experiments should be closely examined when interpreting the data.

## ACKNOWLEDGMENTS

This work was supported by the National Natural Science Foundation of China Grant No. 11772284.

## REFERENCES

- <sup>1</sup>R. D. Richtmyer, “Taylor instability in shock acceleration of compressible fluids,” *Commun. Pure Appl. Math.* **13**, 297–319 (1960).
- <sup>2</sup>E. E. Meshkov, “Instability of the interface of two gases accelerated by a shock wave,” *Fluid Dyn.* **4**, 101–104 (1969).
- <sup>3</sup>F. Marble, G. Hendricks, and E. Zukoski, “Progress toward shock enhancement of supersonic combustion processes,” in *23rd AIAA, SAE, ASME, and ASEE, Joint Propulsion Conference, San Diego, CA, 29 June–2 July 1987* (American Institute of Aeronautics and Astronautics, New York, 1987), p. 1.
- <sup>4</sup>W. D. Arnett, J. N. Bahcall, R. P. Kirshner, and S. E. Woosley, “Supernova 1987A,” *Annu. Rev. Astron. Astrophys.* **27**, 629–700 (1989).
- <sup>5</sup>J. D. Lindl, R. L. McCrory, and E. M. Campbell, “Progress toward ignition and burn propagation in inertial confinement fusion,” *Phys. Today* **45**, 32–40 (1992).
- <sup>6</sup>N. J. Zabusky, “Vortex paradigm for accelerated inhomogeneous flows: Visio-metrics for the Rayleigh–Taylor and Richtmyer–Meshkov environments,” *Annu. Rev. Fluid Mech.* **31**, 495–536 (1999).
- <sup>7</sup>M. Brouillette, “The Richtmyer–Meshkov instability,” *Annu. Rev. Fluid Mech.* **34**, 445–468 (2002).
- <sup>8</sup>D. Ranjan, J. Oakley, and R. Bonazza, “Shock-bubble interactions,” *Annu. Rev. Fluid Mech.* **43**, 117–140 (2011).
- <sup>9</sup>K. A. Meyer and P. J. Blewett, “Numerical investigation of the stability of a shock accelerated interface between two fluids,” *Phys. Fluids* **15**, 753–759 (1972).
- <sup>10</sup>M. A. Jones and J. W. Jacobs, “A membraneless experiment for the study of Richtmyer–Meshkov instability of a shock-accelerated gas interface,” *Phys. Fluids* **9**, 3078–3085 (1997).
- <sup>11</sup>O. Sadot, L. Erez, U. Alon, D. Oron, L. A. Levin, G. Erez, G. Ben-Dor, and D. Shvarts, “Study of nonlinear evolution of single-mode and two-bubble interaction under Richtmyer–Meshkov instability,” *Phys. Rev. Lett.* **80**, 1654–1657 (1998).
- <sup>12</sup>B. D. Collins and J. W. Jacobs, “PLIF flow visualization and measurements of the Richtmyer–Meshkov instability of an air/SF<sub>6</sub> interface,” *J. Fluid Mech.* **464**, 113–136 (2002).
- <sup>13</sup>A. Rikanati, D. Oron, O. Sadot, and D. Shvarts, “High initial amplitude and high Mach number effects on the evolution of the single-mode Richtmyer–Meshkov instability,” *Phys. Rev. E* **67**, 026307 (2003).
- <sup>14</sup>J. F. Haas and B. Sturtevant, “Interaction of weak shock waves with cylindrical and spherical gas inhomogeneities,” *J. Fluid Mech.* **181**, 41–76 (1987).
- <sup>15</sup>J. W. Jacobs, “Shock-induced mixing of a light-gas cylinder,” *J. Fluid Mech.* **234**, 629–649 (1992).
- <sup>16</sup>J. J. Quirk and S. Karni, “On the dynamics of a shock-bubble interaction,” *J. Fluid Mech.* **318**, 129–163 (1996).
- <sup>17</sup>J. S. Bai, L. Y. Zou, T. Wang, and K. Liu, “Experimental and numerical study of shock-accelerated elliptic heavy gas cylinders,” *Phys. Rev. E* **82**, 056318 (2010).
- <sup>18</sup>D. Li, G. Wang, and B. Guan, “On the circulation prediction of shock-accelerated elliptical heavy gas cylinders,” *Phys. Fluids* **31**, 056104 (2019).
- <sup>19</sup>Z. Zhai, M. Wang, T. Si, and X. Luo, “On the interaction of a planar shock with a light polygonal interface,” *J. Fluid Mech.* **757**, 800–816 (2014).
- <sup>20</sup>X. Luo, M. Wang, T. Si, and Z. Zhai, “On the interaction of a planar shock with an SF<sub>6</sub> polygon,” *J. Fluid Mech.* **773**, 366–394 (2015).
- <sup>21</sup>E. Fan, B. Guan, C.-Y. Wen, and H. Shen, “Numerical study on the jet formation of simple-geometry heavy gas inhomogeneities,” *Phys. Fluids* **31**, 026103 (2019).
- <sup>22</sup>X. Luo, P. Dong, T. Si, and Z. Zhai, “The Richtmyer–Meshkov instability of a ‘V’ shaped air/SF<sub>6</sub> interface,” *J. Fluid Mech.* **802**, 186–202 (2016).
- <sup>23</sup>Z. Zhai, P. Dong, T. Si, and X. Luo, “The Richtmyer–Meshkov instability of a ‘V’ shaped air/helium interface subjected to a weak shock,” *Phys. Fluids* **28**, 082104 (2016).
- <sup>24</sup>X. Luo, Y. Liang, T. Si, and Z. Zhai, “Effects of non-periodic portions of interface on Richtmyer–Meshkov instability,” *J. Fluid Mech.* **861**, 309–327 (2019).
- <sup>25</sup>L. Liu, Y. Liang, J. Ding, N. Liu, and X. Luo, “An elaborate experiment on the single-mode Richtmyer–Meshkov instability,” *J. Fluid Mech.* **853**, R2 (2018).
- <sup>26</sup>Y. Liang, Z. Zhai, J. Ding, and X. Luo, “Richtmyer–Meshkov instability on a quasi-single-mode interface,” *J. Fluid Mech.* **872**, 729–751 (2019).
- <sup>27</sup>G. Layes, G. Jourdan, and L. Houas, “Distortion of a spherical gaseous interface accelerated by a plane shock wave,” *Phys. Rev. Lett.* **91**, 174502 (2003).
- <sup>28</sup>J. H. J. Niederhaus, J. A. Greenough, and J. G. Oakley, “A computational parameter study for the three-dimensional shock bubble interaction,” *J. Fluid Mech.* **594**, 85–124 (2008).
- <sup>29</sup>A. Yosef-Hai, O. Sadot, D. Kartoon, D. Oron, L. A. Levin, E. Sarid, Y. Elbaz, G. Ben-dor, and D. Shvarts, “Late-time growth of the Richtmyer–Meshkov instability for different Atwood numbers and different dimensionalities,” *Laser Part. Beams* **21**, 363–368 (2003).
- <sup>30</sup>P. R. Chapman and J. W. Jacobs, “Experiments on the three-dimensional incompressible Richtmyer–Meshkov instability,” *Phys. Fluids* **18**, 074101 (2006).
- <sup>31</sup>C. C. Long, V. V. Krivets, J. A. Greenough, and J. W. Jacobs, “Shock tube experiments and numerical simulation of the single-mode, three dimensional Richtmyer–Meshkov instability,” *Phys. Fluids* **21**, 114104 (2009).
- <sup>32</sup>B. Thornber, D. Drikakis, D. L. Youngs, and R. J. R. Williams, “Physics of the single-shocked and reshocked Richtmyer–Meshkov instability,” *J. Turbul.* **13**, N10 (2012).
- <sup>33</sup>B. Thornber, J. Griffond, P. Bigdelou, I. Boureima, P. Ramaprabhu, O. Schilling, and R. J. R. Williams, “Turbulent transport and mixing in the multimode narrow-band Richtmyer–Meshkov instability,” *Phys. Fluids* **31**, 096105 (2019).
- <sup>34</sup>J. R. Ristorcelli, A. A. Gowardhan, and F. F. Grinstein, “Two classes of Richtmyer–Meshkov instabilities: A detailed statistical look,” *Phys. Fluids* **25**, 044106 (2013).
- <sup>35</sup>D. J. Hill, C. Pantano, and D. I. Pullin, “Large-eddy simulation and multiscale modelling of a Richtmyer–Meshkov instability with reshock,” *J. Fluid Mech.* **557**, 29–61 (2006).
- <sup>36</sup>V. G. Weirs, T. Dupont, and T. Plewa, “Three-dimensional effects in shock-cylinder interactions,” *Phys. Fluids* **20**, 044102 (2008).
- <sup>37</sup>J. Ding, Y. Liang, M. Chen, Z. Zhai, T. Si, and X. Luo, “Interaction of planar shock wave with three-dimensional heavy cylindrical bubble,” *Phys. Fluids* **30**, 106109 (2018).
- <sup>38</sup>R. Krechetnikov, “Rayleigh–Taylor and Richtmyer–Meshkov instabilities of flat and curved interfaces,” *J. Fluid Mech.* **625**, 387–410 (2009).
- <sup>39</sup>X. Luo, X. Wang, and T. Si, “The Richtmyer–Meshkov instability of a three dimensional air/SF<sub>6</sub> interface with a minimum-surface feature,” *J. Fluid Mech.* **722**, R2 (2013).
- <sup>40</sup>X. Luo, B. Guan, T. Si, Z. Zhai, and X. Wang, “Richtmyer–Meshkov instability of a three-dimensional SF<sub>6</sub>–air interface with a minimum-surface feature,” *Phys. Rev. E* **93**, 013101 (2016).
- <sup>41</sup>X. Luo, B. Guan, Z. Zhai, and T. Si, “Principal curvature effects on the early evolution of three-dimensional single-mode Richtmyer–Meshkov instabilities,” *Phys. Rev. E* **93**, 023110 (2016).
- <sup>42</sup>B. Guan, Z. Zhai, T. Si, X. Lu, and X. Luo, “Manipulation of three-dimensional Richtmyer–Meshkov instability by initial interfacial principal curvatures,” *Phys. Fluids* **29**, 032106 (2017).



- <sup>43</sup>S. Osher and J. A. Sethian, "Fronts propagating with curvature-dependent speed: Algorithms based on Hamilton-Jacobi formulations," *J. Comput. Phys.* **79**, 12–49 (1988).
- <sup>44</sup>C. W. Wang, T. G. Liu, and B. C. Khoo, "A real ghost fluid method for the simulation of multimediuim compressible flow," *SIAM J. Sci. Comput.* **28**, 278–302 (2006).
- <sup>45</sup>G. Jiang and C. Shu, "Efficient implementation of weighted ENO schemes," *J. Comput. Phys.* **126**, 202–228 (1996).
- <sup>46</sup>B. Ira, "The science of soap films and soap bubbles," *J. Chem. Educ.* **58**, A179 (1981).
- <sup>47</sup>Z. Zhai, T. Si, X. Luo, and J. Yang, "On the evolution of spherical gas interfaces accelerated by a planar shock wave," *Phys. Fluids* **23**, 084104 (2011).
- <sup>48</sup>M. Wang, T. Si, and X. Luo, "Generation of polygonal gas interfaces by soap film for Richtmyer-Meshkov instability study," *Exp. Fluids* **54**, 1427 (2013).